

**Room temperature ferromagnetism in MoTe<sub>2</sub> by post-growth incorporation of vanadium impurities**

Coelho, P. M.; Komsa, H.-P.; Lasek, K.; Kalappattil, V.; Karthikeyan, J.; Phan, M.-H.; Krasheninnikov, A.; Batzill, M.;

Originally published:

April 2019

**Advanced Electronic Materials 5(2019)5, 1900044**

DOI: <https://doi.org/10.1002/aelm.201900044>

Perma-Link to Publication Repository of HZDR:

<https://www.hzdr.de/publications/Publ-29161>

Release of the secondary publication  
on the basis of the German Copyright Law § 38 Section 4.

## Room temperature ferromagnetism in MoTe<sub>2</sub> by post-growth incorporation of vanadium impurities

Paula Mariel Coelho,<sup>1</sup> Hannu-Pekka Komsa,<sup>2</sup> Kinga Lasek,<sup>1</sup> Vijaysankar Kalappattil,<sup>1</sup> Jeyakumar Karthikeyan,<sup>2</sup> Manh-Huong Phan,<sup>1</sup> Arkady V Krasheninnikov,<sup>2,3</sup> Matthias Batzill<sup>1,\*</sup>

1. Department of Physics, University of South Florida, Tampa, FL 33620, USA

2. Department of Applied Physics, Aalto University, 00076 Aalto, Finland

3. Institute of Ion Beam Physics and Materials Research, Helmholtz-Zentrum Dresden-Rossendorf, 01328 Dresden, Germany

### Abstract:

Post-synthesis doping of two-dimensional (2D) materials is demonstrated by incorporation of vapor deposited transition metals into the MoTe<sub>2</sub> lattice. Using this approach, vanadium-doping of 2H-MoTe<sub>2</sub> produces a 2D ferromagnetic semiconductor with a Curie temperature above room temperature (RT). Surprisingly, the ferromagnetic properties can be induced with very low vanadium concentrations down to ~0.2%. The vanadium species introduced at RT are metastable, and annealing to above ~500 K results in the formation of a thermodynamically favored impurity configuration that, however, exhibit reduced ferromagnetic properties. Doping with titanium, instead of vanadium, shows a similar incorporation behavior, but no ferromagnetism is induced in MoTe<sub>2</sub>. This indicates that the type of impurities in addition to their atomic configurations is responsible for the induced magnetism. The interpretation of the experimental results is consistent with *ab-initio* calculations, which confirm that the proposed vanadium-impurity configurations exhibit magnetic moments, in contrast to the same configurations with titanium-impurities. This study illustrates the possibility to induce ferromagnetic properties in layered van der Waals semiconductors by controlled magnetic impurity doping and thus to add magnetic functionalities to 2D materials.

**Keywords:** 2D Materials, magnetism, MoTe<sub>2</sub>, dopants, impurities, diluted ferromagnet

Weak interactions between structural units in van der Waals (vdW) heterostructures allow combinations of materials with different properties and limited interlayer electronic hybridization. Two-dimensional (2D) ferromagnetic materials are desirable for exploring magnetic coupling in vdW heterostructures, and potentially to exploit them in spintronics applications. Such potential applications of magnetic vdW materials have recently sparked considerable interest in investigating magnetism of bulk ferromagnetic materials thinned to a single layer<sup>1,2,3,4</sup> or the emergence of ferromagnetism of paramagnetic bulk materials at the monolayer limit.<sup>5,6</sup> In addition, defect- and dopant-induced ferromagnetism has been predicted theoretically.<sup>7,8,9,10,11,12</sup> Recent experimental results suggest that 1T-2H phase boundaries in MoSe<sub>2</sub>,<sup>13,14</sup> edges in WS<sub>2</sub> or MoS<sub>2</sub>,<sup>15,16,17,18</sup> or substitutional doping of transition metals in 2D materials<sup>19,20,21</sup> can result in defect- or dopant-induced ferromagnetic ordering in these systems. Recently, long-range magnetic order has also been observed in both MoTe<sub>2</sub> and MoSe<sub>2</sub>, which has been suggested to be induced by intrinsic ferromagnetic defects, such as Mo antisites, i.e. Mo-atoms at chalcogen lattice-sites.<sup>22</sup> This indicates that in these materials even dilute defects can cause long-range ferromagnetic ordering, making them promising diluted magnetic semiconductor (DMS) materials. Here we investigate a new doping mechanism for 2H-MoTe<sub>2</sub> that enables altering the monolayer or surface layer of a MoTe<sub>2</sub> crystal with transition metal impurities. We have recently demonstrated that 2H-MoTe<sub>2</sub> and MoSe<sub>2</sub> can be modified by incorporation of transition metals into the host's interstitial site.<sup>23</sup> We have shown experimentally and by density-functional theory (DFT) calculations that excess Mo-atoms on MoTe<sub>2</sub> are energetically favored at interstitial sites as compared to adsorbed atoms at the surface. At elevated temperatures these excess transition metal atoms are mobile and can undergo site-exchange with lattice Mo-atoms. For high enough mobility (temperature) the interstitials re-arrange into one-dimensional Mo-rich crystal modifications, known as mirror twin grain boundaries.<sup>24,25,26</sup> These grain boundaries have shown no ferromagnetic properties. We demonstrate here, that this doping mechanism can also be expanded to other transition metals, in particular with the goal of inducing magnetism into MoTe<sub>2</sub>. Titanium or vanadium has been used as ferromagnetic dopants in diluted semiconductor systems<sup>27,28</sup> and thus, in this study we explore if V can be introduced into MoTe<sub>2</sub> interstitial sites or as substitutional impurities (at Mo- or Te-sites) and if these magnetic dopants can cause ferromagnetic ordering in MoTe<sub>2</sub>.

Commercially available synthetically grown 2H-MoTe<sub>2</sub> single crystals were cleaved in air and introduced immediately into an ultra-high vacuum (UHV) chamber. The crystal was characterized by scanning tunneling microscopy (STM), as shown in Fig. 1. On small-scale images, atomic defects are observed that are characterized in STM as very weak protrusions extending over a few unit cells, but are present in very low concentrations in our samples, as shown in Fig. 1(a). This is similar to previously reported STM images

and was suggested to be due to antisite defects, i.e. Mo in a Te-site.<sup>22</sup> Annealing of these substrates to above 500 K in ultrahigh vacuum (UHV) causes the formation of additional defects on the surface. The center of these defects coincides with the Te-lattice sites and are identified as Te-vacancies, as confirmed by DFT simulations discussed below. The magnetic properties of these and other samples are characterized with a vibrating sample magnetometer (VSM). The as received MoTe<sub>2</sub> single crystal exhibits a very weak ferromagnetic signal on its diamagnetic background, as shown in the magnetization versus magnetic field (M-H) plot in Fig. 1(a) with the background subtracted. Information on the background subtraction are shown in the supplemental information (Fig. S1). Annealing and introduction of Te-vacancies does not change the magnetic properties of MoTe<sub>2</sub>, shown in Fig. 1(b).

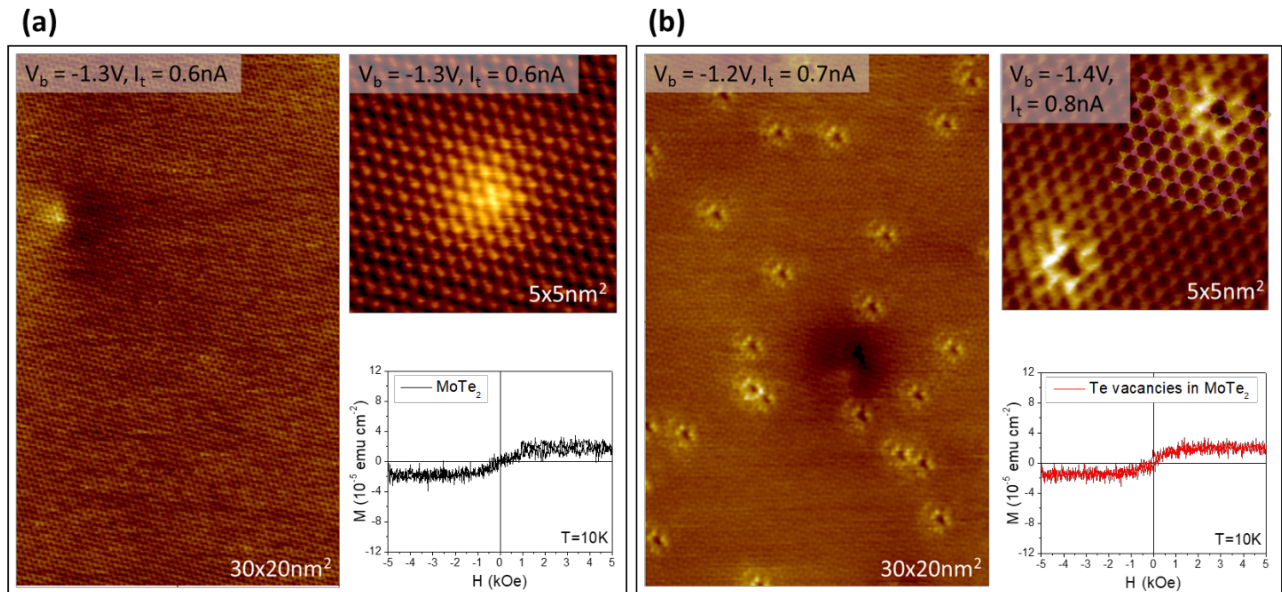


**Fig. 1: Room temperature STM images and related magnetization versus magnetic field (M-H) measurements at 10 K for (a) clean MoTe<sub>2</sub> single crystal with few weak protrusions and (b) MoTe<sub>2</sub> with additional Te vacancies created by vacuum annealing of the crystal to above 500 K. All the magnetic measurements were performed with the samples protected by a ~ 10nm thick Te capping layer.**

In order to investigate possible formation of 2D- DMS, Ti- or V- has been vapor deposited onto MoTe<sub>2</sub> surface from a water cooled mini e-beam evaporators with the sample held at room temperature (RT). Figure 2 shows STM images of ~ 0.3% of a monolayer (ML) of V deposited on MoTe<sub>2</sub>. Here we define ML as equivalent to one atom per MoTe<sub>2</sub> unit cell, and the coverage was estimated from counting protrusions in STM images after deposition. The sample is covered with mostly uniformly sized bright protrusions, in addition to a few larger 'clusters'. The protrusions exhibit a height of only ~ 2 Å and thus could be due to

electronic effects of metallic impurities in the semiconducting MoTe<sub>2</sub> and not a topographical feature, e.g., adatoms. Unfortunately, no atomic detail was possible to obtain for these small protrusions or their surrounding lattice. Metal adatoms are, however, expected to be mobile and agglomerate into large metal clusters at the surface, which has been also confirmed by estimating diffusion barriers of metal adatoms by DFT simulations (supplemental information). Also, the samples were found to be stable in air. Fig. 2 (b) shows a sample after removal from the vacuum vessel for magnetic measurements (presented below) and then reintroducing into the vacuum system for STM imaging. The main structural difference appears to be for the few larger ‘clusters’ that after air-exposure show a dark depression in their center. The stability of the small protrusions to air-exposure is further evidence that these cannot be single V-adatoms or V-clusters as those would oxidize and/or agglomerate. Consequently, these must be strongly bound V-atoms incorporated into the MoTe<sub>2</sub> atomic network.

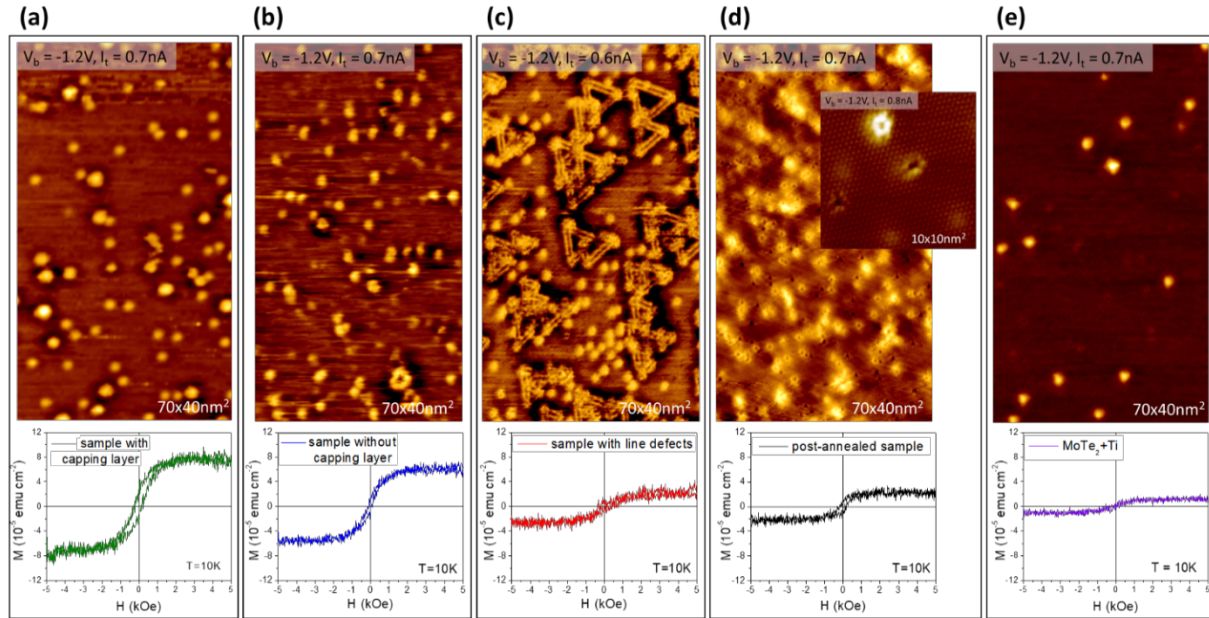


**Fig. 2: RT-STM images and related M-H hysteresis loops taken at 10K. 0.3% of a monolayer of V deposited at RT in MoTe<sub>2</sub> (a) before and (b) after exposure to air. (c) V deposited at 600K in MoTe<sub>2</sub>, presenting mirror twin grain boundaries defects and (d) deposited at RT with subsequent annealing at 600K, presenting small bright triangular loops and Te vacancies. (e) Ti deposited at RT on MoTe<sub>2</sub>.**

Deposition V at elevated temperatures (600 K) results in the formation of mirror twin boundaries (MTBs) between the grains, as shown in Fig. 2(c), which suggests high mobility of the deposited metals. This is similar to what we have reported previously for Mo-deposition.<sup>23</sup> In contrast, annealing of samples with RT deposited V to 500-600K does not cause a massive restructuring into MTBs, but a transformation of

the V-induced defects is observed nevertheless. The single bright protrusions observed after RT-deposition disappear and instead a small bright triangular loop appears. At the same time, as discussed above, more Te-vacancies form at this annealing temperature. Thus, post-deposition annealing results into two discernable defect structures as shown in the inset of Fig. 2 (d). From DFT calculations discussed below we identify both defect structures as associated with Te-vacancies, with the brighter defect being a Te-vacancy modified by charge transfer from an adjacent V-interstitial atom.

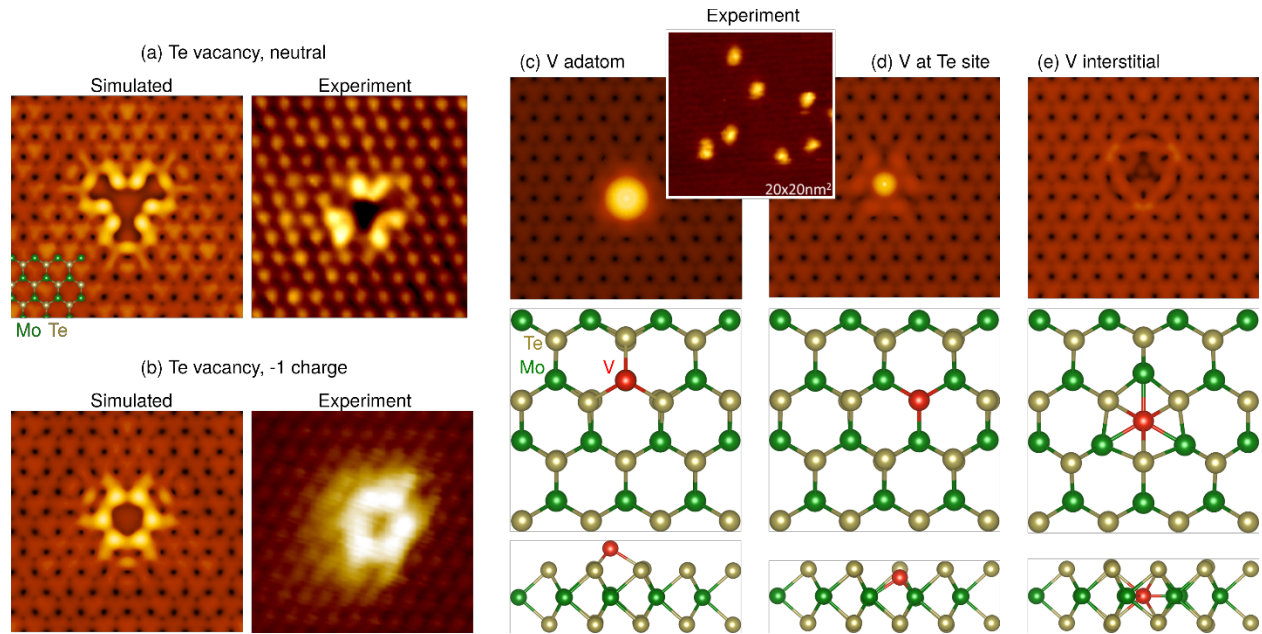
Both the as-prepared samples and those capped with a few nanometer thick tellurium layer were characterized for their magnetic properties. The Te-capping helps protect the surface of MoTe<sub>2</sub> from adsorbates and reactions with the atmosphere. Importantly, both samples (with or without) capping showed enhanced ferromagnetic properties as compared to the samples without V-dopants. However, there are variations in the saturation magnetization and coercive field, as can be seen from comparison of the M-H curves in Fig. 2 (a) and (b). These reductions of the magnetic properties for the unprotected surface is likely a consequence of adsorption of molecules. These adsorbates may interact with defect/dopants or induce a band bending at the surface of MoTe<sub>2</sub> and thus change the charge carrier concentration in the surface layer. While the observed variations in the magnetic properties of doped MoTe<sub>2</sub> surface may hint the tunability of the magnetic properties by its environment or by field induced band bending, this cannot be conclusively established by the uncontrolled exposure to air and is beyond the scope of this paper. The important point for this paper is that the Te-capping layer is not a critical component for inducing magnetism in this system, and we consider it as a passive protective layer, which we employed for all other studies to avoid uncontrollable influences from surface adsorbates/contaminations.

The magnetic properties of the V-modified surfaces depend on the atomic configuration of V dopants. Only samples prepared at RT, and thus exhibiting the single protrusions, exhibit clear M-H hysteresis loops, while after annealing the saturation magnetization is strongly suppressed, as shown in Fig. 2 (c), and only remains slightly larger than that of MoTe<sub>2</sub> (Fig. 1(a)). This suggests that only the metastable V-species that are observed after the RT preparation are magnetically active, and the annealing promotes a transition into lower energy configurations, which appear to be non-magnetic. Also, samples prepared by the post-growth incorporation of Ti show an almost identical M-H hysteresis loop, as compared to pure MoTe<sub>2</sub> (compare Fig. 2 (e) with Fig. 1(a)), thus indicating that the magnetic properties are caused by V-dopants and not by any other intrinsic defects that may form during the deposition of transition metals.

**Table 1: Formation energy ( $E_f$  in eV) and magnetic moment ( $M$  in  $\mu_B$ ) of different atomic configurations of Ti and V atom in  $\text{MoTe}_2$  layer.**

Configuration	X=Ti		X=V	
	$E_f$ (eV)	$M$ ( $\mu_B$ )	$E_f$ (eV)	$M$ ( $\mu_B$ )
Adatom	-0.555	4.00	-1.126	5.00
Interstitial	-3.139	0.00	-3.569	1.00
X at Mo site + Mo interstitial	-3.332	0.00	-2.947	0.00
(X-Mo) split	-0.029	0.00	-0.626	0.00
X at Te site + Te adatom	-1.651	1.91	-1.884	0.00
X at Te site	-4.248	0.00	-3.758	1.00
X at Mo site	-0.972	1.00	-1.153	0.00

To assign the features observed in STM images to specific atomic configurations involving defects and impurity atoms, we conducted systematic DFT studies of the formation energies  $E_f$  and simulated STM images of V atoms incorporated at various lattice and interstitial sites.  $E_f$  and magnetic moments for selected V and Ti defects are listed in Table 1 (see SI for a more complete list and for the atomic structures). While the deposited metal atoms are initially likely to be adsorbed on the surface, there exists several other sites with energy lower than that for adatoms. In particular, the lowest energy configuration for an additional V atom is in the interstitial site. If Te vacancies are present, transition metal adatoms can fill them up, which would also provide magnetic moment for V, but not for Ti. Mo-site substitution is unlikely, since we did not observe Mo vacancies in the freshly cleaved samples and V at Mo-sites has zero magnetic moment, while Ti at such sites would exhibit a magnetic moment, i.e. behave opposite to our observations.



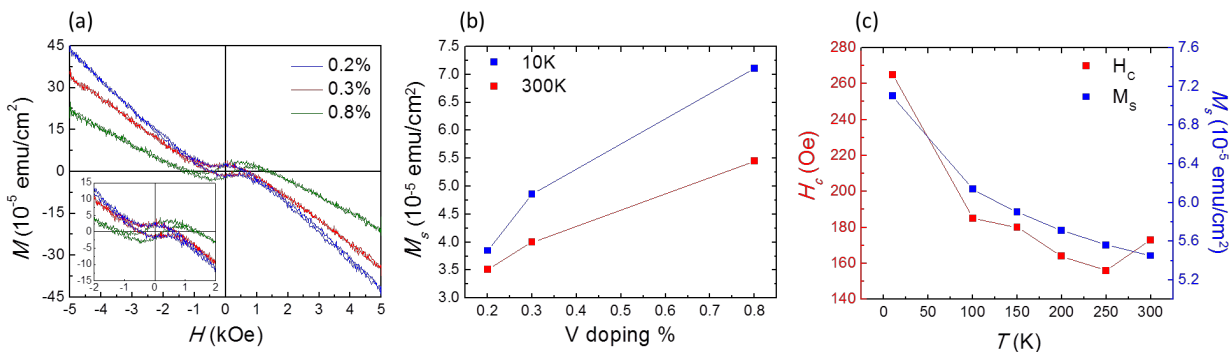
**Fig. 3: Simulated STM images and comparison to experimental images for (a,b) Te vacancy in the neutral and -1 charge states, (c) V adatom, (d) V at Te site, and (e) V interstitial. For the last three, the atomic structures are also shown below the STM images. The inset between (c) and (d) presents the experimental STM image of the bright protrusions for reference, but lacks atomic resolution.**

Fig. 3 shows the simulated STM images for neutral and negatively charged Te vacancy, V adatom, V at a Te site, and V in an interstitial-site. We obtain good agreement with vacuum-annealed samples where Te vacancies are expected (Fig.3 (a)). For V deposited at RT, we only observe single bright protrusions in the experiments, which are naturally obtained in the simulations for defects with protruding atoms, such as adatoms. However, V adatoms have already been ruled out due to their expected mobility (see supplement) and expected instability in air. Thus, a more likely match for the protrusion is given by V (or Ti) at a Te-site (Fig. 3(d)). Importantly, V at Te-sites also exhibits a magnetic moment of  $1 \mu_B$ , while Ti has no magnetic moment, suggesting that only V could induce magnetism in this system, which is in agreement with the experiments. However, V atom at the Te site has a fairly small barrier for migration to an interstitial position, so that this configuration is metastable and will change to the thermodynamically preferred interstitial site at elevated temperature, leaving a Te-vacancy at the surface. In accordance with this scenario, the best agreement of the prominent defect structure observed in STM is obtained for negatively charged Te vacancies, see Fig. 3(b). The negative charging of the Te-vacancy is consistent with V interstitials acting as donors and Te vacancies as acceptors. It is also noteworthy, that

neutral V in interstitial sites would exhibit a magnetic moment, but if it donates its electron to a Te-vacancy, it becomes non-magnetic. It is this interplay between V-interstitials and Te-vacancies that explains the transition from magnetic to non-magnetic properties upon annealing. Interestingly, the proposed magnetic configuration of a V at Te-site is similar to the Mo-antisite defect that has been suggested to be responsible for long range magnetic order in MoTe<sub>2</sub>.<sup>22</sup> For completeness, we mention that the contrast for a V interstitial is very low and thus cannot explain the bright protrusions nor the bright ‘rings’ observed in STM images, see Fig. 3(e). We have considered several other possible structures with none of them being in agreement with the experiments (see SI).

To further experimentally evaluate the magnetic characteristics of V-modified MoTe<sub>2</sub>, we conducted V-coverage- and temperature-dependent M-H measurements. In Fig. 4, we compare samples within the accessible concentration range before clustering of V adatoms at the surface occurs. This limits us to low V-concentrations, and we measure samples with ~0.2 %, 0.3 % and 0.8 % V concentration. Fig. 4 (a) shows a comparison of raw M-H loops for differently doped samples at 10 K normalized to the sample surface area only. The weak signal and the complexity of the system with both diamagnetic and paramagnetic contributions makes a background subtraction from the ferromagnetic signal difficult and we show in the supplement that a commonly used linear subtraction of a diamagnetic background may result in erroneous results. Therefore, we extract values for  $M_s$  and  $H_c$  directly from the raw data without background subtraction as illustrated in Fig. S1. With increased doping an increase in  $M_s$  is observed while  $H_c$  remains unchanged within the accuracy of the measurement. Although  $M_s$  increases roughly proportional to the V-dopant concentration (Fig. 4 (b)), it appears that the measured  $M_s$  cannot be only associated with the magnetic moments of the V-dopants (in fact it would be beyond the sensitivity of the VSM to pick up magnetism for such low V concentration) and thus we conclude that the V impurities must cause some magnetic polarization of MoTe<sub>2</sub>, similar to what has recently been shown for intrinsic defect-induced ferromagnetic ordering in MoTe<sub>2</sub>.<sup>22</sup> This points towards a different mechanism for the observed ferromagnetic ordering than the models proposed in carrier-mediated semiconducting<sup>29,30</sup> or polaron-mediated oxide<sup>28</sup> DMS systems. However, further tests such as field effect gating would be required to study the role of charge carriers in this system.<sup>31</sup> The temperature dependence of  $M_s$  and  $H_c$  for the 0.8% doped sample is shown in Fig. 4 (c). A weak decrease of  $M_s$  with increasing T in the accessible temperature range indicates a high Curie temperature above RT. The  $H_c$  remains constant within the experimental uncertainty up to ~ 100 K and only for the lowest temperature of 10 K an experimentally significant increase in  $H_c$  is observed. The increase of  $H_c$  at low T may suggest a transition to a longer range magnetic coupling due to reduced thermal excitations. We stress that the technologically most important

observation is that the magnetization persists to above 300 K. This is a much higher Curie temperature than in typical DMS systems and is also higher than the  $\sim 100$  K reported for  $\text{MoTe}_2$  promoted by intrinsic defects.<sup>22</sup>



**Fig. 4 Magnetization measurements of  $\text{MoTe}_2$  with different V concentrations. (a) M-H hysteresis loops taken at 10K for  $\text{MoTe}_2$  with 0.2%, 0.3%, and 0.8% of V coverage. The variation of the linear diamagnetic background is a consequence of different substrate thicknesses. (b) Variation in magnetization saturation with the V-concentration. (c) Temperature dependences of  $H_c$  and  $M_s$  for the 0.8% V-doped sample.**

In conclusion, we identify V-doped  $\text{MoTe}_2$  as a new RT ferromagnet. The incorporation of V into pristine  $\text{MoTe}_2$  is a post-growth process, and this will allow us to modify  $\text{MoTe}_2$  sheets locally, by, e.g., shadow mask deposition or other directed deposition methods. Importantly, this doping mechanism may introduce metastable configurations that are difficult to synthesize during the growth of such materials that tend to favor the thermodynamically stable configurations, which, as we have shown, may not introduce ferromagnetic ordering. Recent developments in the control of magnetism in 2D materials by electric field<sup>32</sup> may also enable modifying the magnetic properties in the V: $\text{MoTe}_2$  system by external stimuli, and this may also be a way to gain better fundamental understanding of the magnetic exchange coupling in this material, specifically to get insights into the potential role of charge carriers. Moreover, magnetic properties complement electrostatic doping-induced structural phase change from H- to 1T' phases<sup>33</sup> and thus make  $\text{MoTe}_2$  an important switchable multifunctional material.

#### Associated Content:

The supporting information is available free of charge on the ACS publication website at DOI: XXXXXXXX. SI contains description of data analysis of M-H hysteresis loops and procedures of background subtraction. Details of DFT simulations, full list and results for all defect configurations considered, and estimates for migration barriers of V ad-atoms, as well as local density of states for pertinent dopant configurations.

**Author information:**

Corresponding author:

\*e-mail: mbatzill@usf.edu

**Acknowledgement:** Financial support from the National Science Foundation under grant DMR-1701390 and CHE-1801199 is acknowledged. We are grateful to the Academy of Finland for the support under Projects No.286279 and 311058. We also thank CSC-IT Center for Science Ltd., Finland for generous grants of computer time. M.-H. P. acknowledges support from the U.S. Department of Energy, Office of Basic Energy Sciences, Division of Materials Sciences and Engineering under Award No. DE-FG02-07ER46438.

## References:

- 
- <sup>1</sup> Huang, B., Clark, G., Navarro-Moratalla, E., Klein, D.R., Cheng, R., Seyler, K.L., Zhong, D., Schmidgall, E., McGuire, M.A., Cobden, D.H., Yao, W., Xiao, D., Jarillo-Herrero, P., Xu, X. Layer-dependent ferromagnetism in a van der Waals crystal down to the monolayer limit. *Nature* **2017**, 546, 270-273.
- <sup>2</sup> Gong, C., Li, L., Li, Z., Ji, H., Stern, A., Xia, Y., Cao, T., Bao, W., Wang, C., Wang, Y., Qiu, Z. Q., Cava, R. J., Louie, S. G., Xia, J., Zhang, X. Discovery of intrinsic ferromagnetism in two-dimensional van der Waals Crystals. *Nature* **2017**, 546, 265-269.
- <sup>3</sup> Jiang, S., Shan, J., Mak, K.F., Electric-field switching of two-dimensional van der Waals magnets. *Nat. Mater.* **2018**, 17, 406-410.
- <sup>4</sup> Deng, Y., Yu, Y., Song, Y., Zhang, J., Wang, N.Z., Sun, Z., Yi, Y., Wu, Y.Z., Wu, S., Zhu, J., Wang, J., Chen, X.H., Zhang, Y. Gate-tunable room-temperature ferromagnetism in two-dimensional Fe<sub>3</sub>GeTe<sub>2</sub>. *Nature* **2018**, 563, 94–99.
- <sup>5</sup> Bonilla, M., Kolekar, S., Ma, Y., Coy Diaz, H., Kalappattil, V., Das, R., Eggers, T., Gutierrez, H.R., Phan, M.-H., Batzill, M. Strong room-temperature ferromagnetism in VSe<sub>2</sub> monolayers on van der Waals substrates. *Nat. Nano.* **2018**, 13, 289-293.
- <sup>6</sup> O'Hara, D.J., Zhu, T., Trout, A.H., Ahmed, A.S., Luo, Y.K., Lee, C.H., Brenner, M.R., Rajan, S., Gupta, J.A., McComb, D.W., Kawakami R.K. Room Temperature Intrinsic Ferromagnetism in Epitaxial Manganese Selenide Films in the Monolayer Limit. *Nano Lett.* **2018**, 18, 3125–3131.
- <sup>7</sup> Wang, Y., Li, S., Yi, J. Electronic and Magnetic Properties of Co Doped MoS<sub>2</sub> Monolayer. *Sci. Rep.* **6**, 24153 (2016).
- <sup>8</sup> Kumar, P., Skomski, R., Pushpa, R. Magnetically Ordered Transition-Metal-Intercalated WSe<sub>2</sub>. *ACS Omega* **2017**, 2, 7985-7990.
- <sup>9</sup> Zhu, Y., Liang, X., Qin, J., Deng, L., Bi, L. Strain tunable magnetic properties of 3D transition-metal ion doped monolayer MoS<sub>2</sub>: A first-principle study. *AIP Adv.* **2018**, 8, 055917.
- <sup>10</sup> Ramasubramaniam, A., Naveh, D. Mn-doped monolayer MoS<sub>2</sub>: An atomically thin dilute magnetic semiconductor. *Phys. Rev. B* **2013**, 87, 195201.
- <sup>11</sup> Mishra, R., Zhou, W., Pennycook, S.J., Pantelides, S.T., Idrobo, J.-C. Long-Range Ferromagnetic Ordering in Manganese-Doped Two-Dimensional Dichalcogenides. *Phys. Rev. B* **2013**, 88, 144409.
- <sup>12</sup> Ma, X., Zhao, X., Wu, N., Xin, Q., Liu, X., Wang, T., Wei, S. Ferromagnetic properties of Mn-doped HfS<sub>2</sub> monolayer under strain. *Solid State Commun.* **2017**, 268, 15-19.
- <sup>13</sup> Xi, B., Wang, T., Xiao, W., Zheng, R., Liu, P., Ding, J., Gao, D., Xue, D. Phase-transfer induced room temperature ferromagnetic behavior in 1T @ 2H-MoSe<sub>2</sub> nanosheets. *Sci. Rep.* **2017**, 7, 45307.
- <sup>14</sup> Han, S.W., Park, Y., Hwang, Y.H., Jekal, S., Kang, M., Lee, W.G., Yang, W., Lee, G.-D., Hong, S.C. Electron beam-formed ferromagnetic defects on MoS<sub>2</sub> surface along 1T phase transition. *Sci. Rep.* **2016**, 6, 38730 (2016).
- <sup>15</sup> Luxa, J., Jankovsky, O., Sedmidubsky, D., Medlin, R., Marysko, M., Pumera, M., Sofer, Z. Origin of exotic ferromagnetic behavior in exfoliated layered transition metal dichalcogenides MoS<sub>2</sub> and WS<sub>2</sub>. *Nanoscale* **2016**, 8, 1960-1967.
- <sup>16</sup> Zhang, J., Soon, J.M., Loh, K.P., Yin, J., Ding, J., Sullivan, M.B., Wu, P. Magnetic Molybdenum Disulfide Nanosheet Films. *Nano Lett.* **2007**, 7, 2370-2376.
- <sup>17</sup> Zhao, X., Fu, D., Ding, Z., Zhang, Y.-Y., Wan, D., Tan, S.J.R., Chen, Z., Leng, K., Dan, J., Fu, W., Geng, D., Song, P., Du, Y., Venkatesan, T., Pantelides, S.T., Pennycook, S.J., Zhou, W., Loh, K.P. Mo-terminated edge reconstructions in nanoporous molybdenum disulfide film. *Nano Lett.* **2018**, 18, 482–490.

- 
- <sup>18</sup> Vojvodic, A., Hinnemann, B., Nørskov, J.K. Magnetic edge states in MoS<sub>2</sub> characterized using density-functional theory. *Phys. Rev. B* **2009**, 80, 125416.
- <sup>19</sup> Li, B., Xing, T., Zhong, M., Huang, L., Lei, N., Zhang, J., Li, J., Wei, Z. A Two-Dimensional Fe-doped SnS<sub>2</sub> magnetic semiconductor. *Nat. Commun.* **2018**, 8, 1958.
- <sup>20</sup> Ahmed, S., Ding, X., Bao, N., Bian, P., Zheng, R., Wang, Y., Murmu, P. P., Kennedy, J. V., Liu, R., Fan, H., Suzuki, K., Ding, J., Yi, J. Inducing High Coercivity in MoS<sub>2</sub> Nanosheets by Transition Element Doping. *Chem. Mater.* **2017**, 29, 9066-9074.
- <sup>21</sup> Xia, B., Guo, Q., Gao, D., Shi, S., Tao, K. High Temperature Ferromagnetism in Cu-doped MoS<sub>2</sub> Nanosheets. *J. Phys. D: Appl. Phys.* **2016**, 49, 165003.
- <sup>22</sup> Guguchia, Z., Kerelsky, A., Edelberg, D., Banerjee, S., von Rohr, F., Scullion, D., Augustin, M., Scully, M., Rhodes, D.A., Shermadini, Z., Luetkens, H., Shengelaya, A., Baines, C., Morenzoni, E., Amato, A., Hone, J.C., Khasanov, R., Billinge, S.J.L., Santos, E., Pasupathy, A.N., Uemura, Y.J. Magnetism in Semiconducting Molybdenum Dichalcogenides [arXiv:1711.05392](https://arxiv.org/abs/1711.05392)
- <sup>23</sup> Coelho, P.M., Komsa, H.-P., Coy Diaz, H., Ma, Y., Krasheninnikov, A.V., Batzill, M. Post-Synthesis Modifications of Two-Dimensional MoSe<sub>2</sub> or MoTe<sub>2</sub> by Incorporation of Excess Metal Atoms into the Crystal Structure. *ACS Nano* **2018**, 12, 3975–3984.
- <sup>24</sup> Ma, Y., Kolekar, S., Coy Diaz, H., Aprozanz, J., Miccoli, I., Tegenkamp, C., Batzill, M. Metallic Twin Grain Boundaries Embedded in MoSe<sub>2</sub> Monolayers Grown by Molecular Beam Epitaxy. *ACS Nano* **2017**, 11, 5130-5139.
- <sup>25</sup> Ma, Y., Coy Diaz, H., Avila, J., Chen, C., Kalappattil, V., Das, R., Phan, M.-H., Čadež, T., Carmelo, J.M.P., Asensio, M.C., Batzill, M. Angle resolved photoemission spectroscopy reveals spin charge separation in metallic MoSe<sub>2</sub> grain boundary. *Nat. Commun.* **2017**, 8, 14231.
- <sup>26</sup> Batzill, M. Mirror twin grain boundaries in molybdenum dichalcogenides *J. Phys.: Condens. Matter* **2018**, 30, 493001.
- <sup>27</sup> Yun, S. J., Duong, D. L., Doan, M.-H., Singh, K., Phan, T. L., Choi, W., Kim, Y.-M., Lee, Y. H. Room-temperature ferromagnetism in monolayer WSe<sub>2</sub> semiconductor via vanadium dopant. [arXiv:1806.06479](https://arxiv.org/abs/1806.06479)
- <sup>28</sup> Coey, J.M.D., Venkatesan, M., Fitzgerald, C.B. Donor impurity band exchange in dilute ferromagnetic oxides. *Nat. Mater.* **2005**, 4, 173-170.
- <sup>29</sup> Dietl, T., Ohno, H., Matsukura, F., Cibert, J., Ferrand, D. Zener model description of ferromagnetism in zinc-blende magnetic semiconductors. *Science* **2000**, 287, 1019–1022.
- <sup>30</sup> Dietl, T. A ten-year perspective on dilute magnetic semiconductors and oxides. *Nat. Mat.* **2010**, 9, 965- 974.
- <sup>31</sup> Nishitani, Y., Chiba, D., Endo, M., Sawicki, M., Matsukura, F., Dietl, T., Ohno, H. Curie temperature versus hole concentration in field-effect structures of Ga<sub>1-x</sub>MnxAs. *Phys. Rev. B* **2010**, 81, 045208.
- <sup>32</sup> Huang, B., Clark, G., Klein, D.R., MacNeill, D., Navarro-Moratalla, E., Seyler, K.L., Wilson, N., McGuire, M.A., Cobden, D.H., Xiao, D., Yao, W., Jarillo-Herrero, P., Xu, X. Electrical control of 2D magnetism in bilayer CrI<sub>3</sub>. *Nat. Nanotechnol.* **2018**, 13, 544- 548.
- <sup>33</sup> Wang, Y., Xiao, J., Zhu, H., Li, Y., Alsaied, Y., Fong, K.J., Zhou, Y., Wang, S., Shi, W., Wang, Y., Zettl, A., Reed, E.J., Zhang, X. Structural phase transition in monolayer MoTe<sub>2</sub> driven by electrostatic doping. *Nature* **2017**, 550, 487-491.

## Supporting Information:

### Room temperature ferromagnetism in MoTe<sub>2</sub> by post-growth incorporation of vanadium impurities

*Paula Mariel Coelho,<sup>1</sup> Hannu-Pekka Komsa,<sup>2</sup> Kinga Lasek,<sup>1</sup> Vijaysankar Kalappattil,<sup>1</sup> Jeyakumar Karthikeyan,<sup>2</sup> Manh-Huong Phan,<sup>1</sup> Arkady V Krasheninnikov,<sup>2,3</sup> Matthias Batzill<sup>1,\*</sup>*

1. Department of Physics, University of South Florida, Tampa, FL 33620, USA
2. Department of Applied Physics, Aalto University, 00076 Aalto, Finland
3. Institute of Ion Beam Physics and Materials Research, Helmholtz-Zentrum Dresden-Rossendorf, 01328 Dresden, Germany

## Magnetic measurement analysis

For the pristine MoTe<sub>2</sub> single crystals or single crystals modified with Te-vacancies the magnetic M-H curve is dominated by a diamagnetic signal of the bulk MoTe<sub>2</sub> single crystal, see Fig. S1 (a). However, a very weak ferromagnetic contribution is measurable. To emphasize the ferromagnetic signal, a linear diamagnetic background was subtracted. The diamagnetic susceptibility of the substrate was measured at high fields, i.e. where the ferromagnetic contribution is saturated, and the diamagnetic contribution is then subtracted from the raw data (Fig. S1 (b)). This enables us to demonstrate a weak ferromagnetic contribution, without being quantitative about the magnetic properties.

For the V-doped samples, the ferromagnetic contribution is strongly increased, as a comparison of the raw data in Fig. S1 (a) and (c) illustrates. However, to extract quantitative values for  $M_S$  and  $H_C$  a linear background subtraction can cause a non-physical distortion for the weak signals measured in these samples. For instance, Fig. S1 (c) and (d) compare  $M_S$  and  $H_C$  values extracted from the raw data and those after the linear background subtraction. Significantly different values are obtained. In addition to the weak signal, complex diamagnetic and paramagnetic contributions to the total signal may cause a simple linear background subtraction to be inaccurate. Since the ferromagnetic properties are obtained within the low magnetic field range ( $< \pm 1\text{kOe}$ ) where the diamagnetic and paramagnetic effects are less significant, the values of  $M_S$  and  $H_C$  we report in the manuscript are derived from the raw data as illustrated in Fig. S1(c), i.e. taking half of the distance between the magnetic moment maxima as  $M_S$  and the half of the distance between coercive fields maxima as  $H_C$ . To visualize the difference in the value of magnetic moment between clean and V-doped MoTe<sub>2</sub> substrate, Fig. S1 (e) presents comparison between M-H hysteresis loops of MoTe<sub>2</sub> + 0.8% of V before

(green) and after (blue) subtracting the ferromagnetic signal of the substrate.

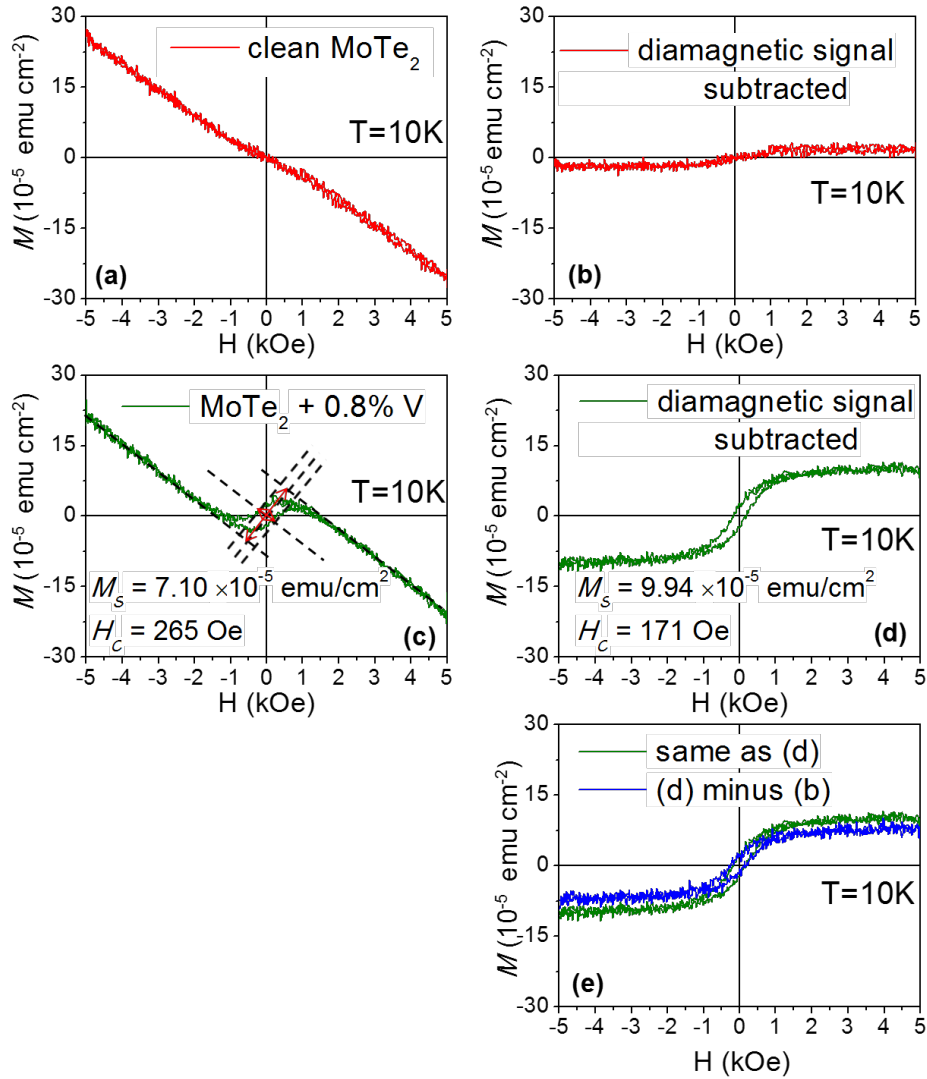


**Figure S1.** Left panels: raw  $M$ - $H$  data of (a) clean  $\text{MoTe}_2$  substrate and (c)  $\text{MoTe}_2 + 0.8\%$  of V coverage. Right panels: after subtracting the major linear component (b) clean  $\text{MoTe}_2$  substrate, (d)  $\text{MoTe}_2 + 0.8\%$  of V coverage and (e) comparison between  $M$ - $H$  hysteresis loops of  $\text{MoTe}_2 + 0.8\%$  of V before (green) and after (blue) subtracting the ferromagnetic signal of the substrate, presenting the magnetization of the  $\text{MoTe}_2 + \text{V}$  surface alone.

## Computational Details

Spin-polarized density functional theory calculations implemented in Vienna Ab-initio Simulation Package (VASP) are employed to understand structure and magnetic properties of Ti and V deposited MoTe<sub>2</sub> single layer. In our calculations, the electron-electrons correlations are described using generalized gradient approach within PBE functionals, and the wave functions are self-consistently optimized with a tight electronic convergence of 10<sup>-6</sup> eV. Without considering any symmetry, all ions are fully relaxed until the final forces on each ion become less than 0.01 eV/Å. To maintain the consistency, a high plane-wave cut-off of 500 eV is used in all the calculations. For this study, a 6×6×1 super-cell was constructed from the optimized unit cell of MoTe<sub>2</sub>. The obtained lattice constants of the unit cell of hexagonal MoTe<sub>2</sub> layer are a = b = 3.550 Å in agreement with the experimentally measured lattice constants. The Brillouin zone of the unit cell and 6×6×1 supercell is sampled with a  $\Gamma$ -centered 13×13×1 and 3×3×1 k-mesh, respectively. In order to calculate a diffusion barrier for the Ti and V atoms, climbing image nudged elastic band method is employed with the same convergence parameters.

For STM image simulations, the defect structures were rebuilt in a larger 10×10×1 supercell due to the large extent of the probed features. Smaller energy cutoff of 400 eV was used, and the Brillouin zone was sampled using only the  $\Gamma$ -point. The calculated formation energies remained nearly unchanged with regard to those obtained in the 6×6×1 super-cell, evidencing that the employed computational parameters are converged. The constant current image simulations were carried out using the P4VASP software. It involves following the isosurface of the partial charge density (here we use isosurface density 3), for which we sum up all the states from Fermi-level down to 0.2 eV below the valence band maximum.

## Formation energies and atomic structures of defects

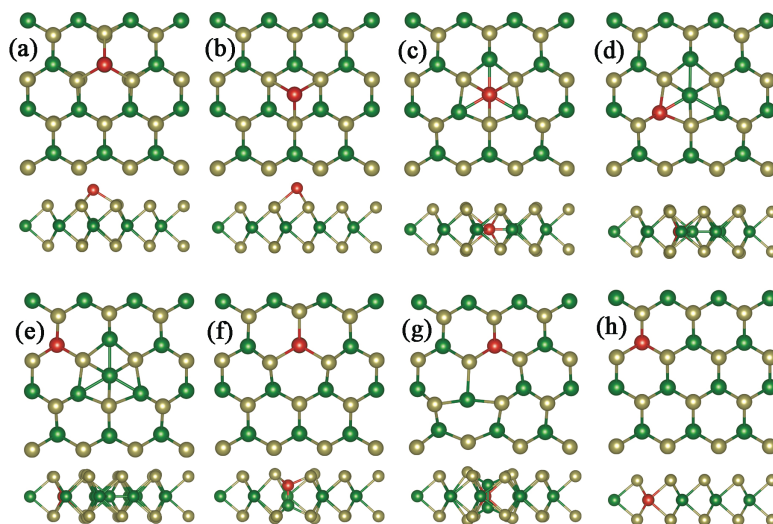


**Figure S2. Representative atomic models for (a) Top-Mo, (b) Top-H, (c) interstitial, (d) split-interstitial, (e) impurity-interstitial-1, (f) impurity-interstitial-2, (g) impurity-split-interstitial and (h) impurity site structure of V or Ti deposited on MoTe<sub>2</sub> layer, top and side views. Throughout this paper, green, ochre and red colored balls represent Mo, Te and V/Ti atoms, respectively.**

For Figure S2(a – g), the formation energy ( $E_f$ ) is calculated using the formula  $E_f = E(\text{MMoTe}_2) - E(\text{M}) - E(\text{MoTe}_2)$ , where  $E(\text{MoTe}_2)$  and  $E(\text{MMoTe}_2)$  are total energy of pristine and metal deposited MoTe<sub>2</sub> layer, respectively, and  $E(\text{M})$  is the chemical potential of a M atom in an isolated M<sub>2</sub> (M=Ti/V) dimer. We chose dimer as a reference system to emphasize the propensity of the metal atoms to form small clusters or impurity/defect

complexes in  $\text{MoTe}_2$ .

For Mo site substitution (shown in 'h'),  $E_f$  is calculated using the formula  $E_f = E(\text{M}_x\text{Mo}_{1-x}\text{Te}_2) - E(\text{M}) + E(\text{Mo}) - E(\text{MoTe}_2)$ , where  $E(\text{MoTe}_2)$  and  $E(\text{M}_x\text{Mo}_{1-x}\text{Te}_2)$  are total energy of pristine and metal substituted  $\text{MoTe}_2$  layer and  $E(\text{M})$  and  $E(\text{Mo})$  are chemical potential of M (M=Ti/V) from  $\text{M}_2$  dimer and that of  $\text{Mo}_2$  dimer, respectively.

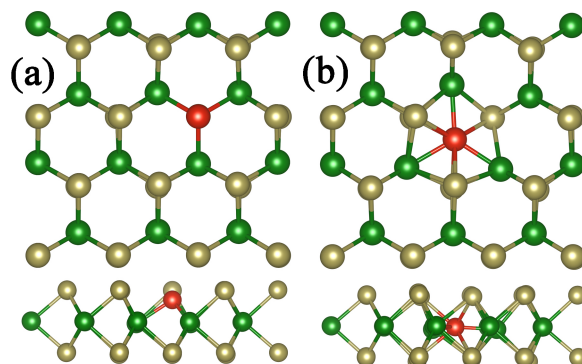


**Figure S3. Representative atomic models for a Ti or V atom occupying (a) Te atom site and (b) a nearest interstitial site of Te defect.**

For Figure S3, the formation energy ( $E_f$ ) is calculated using the formula  $E_f = E(\text{MMoTe}_{2-x}) - E(\text{M}) - E(\text{MoTe}_{2-x})$  where  $E(\text{MoTe}_{2-x})$ , and  $E(\text{MMoTe}_{2-x})$  are total energy of pristine and metal deposited  $\text{MoTe}_2$  layer with a Te vacancy and  $E(\text{M})$  is chemical potential of  $\text{M}_2$  (M=Ti/V) dimer.

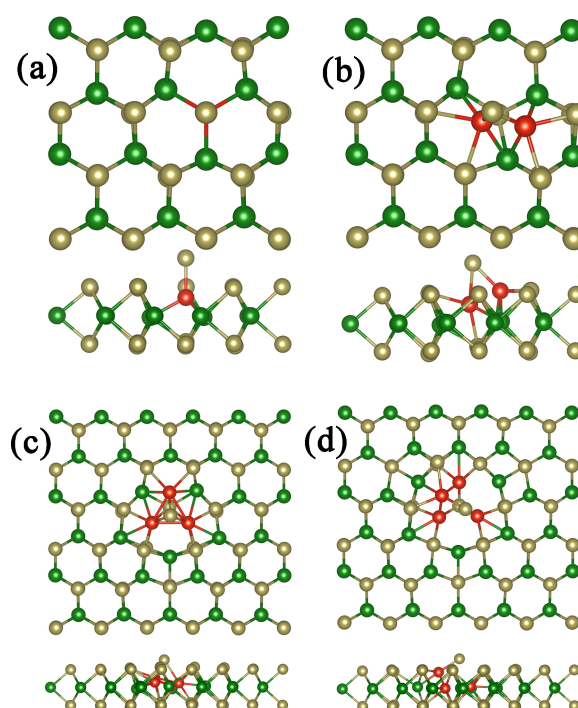


**Figure S4. Representative atomic models for metal-Tellurium (M-Te) surface complex formed with (a) 1M, (b) 2M, (c) 3M and (d) 4M.**

For the surface complex structures in Figure S4, the  $E_f$  is calculated using  $E_f = [E(\text{M}_n\text{MoTe}_2) - nE(\text{M}) - E(\text{MoTe}_2)]/n$ , where  $E(\text{MoTe}_2)$ , and  $E(\text{M}_n\text{MoTe}_2)$  are total energy of pristine and 'n' number of M atom

deposited  $\text{MoTe}_2$  layer and  $E(M)$  is chemical potential of  $M_2$  ( $M=\text{Ti}/\text{V}$ ) dimer.

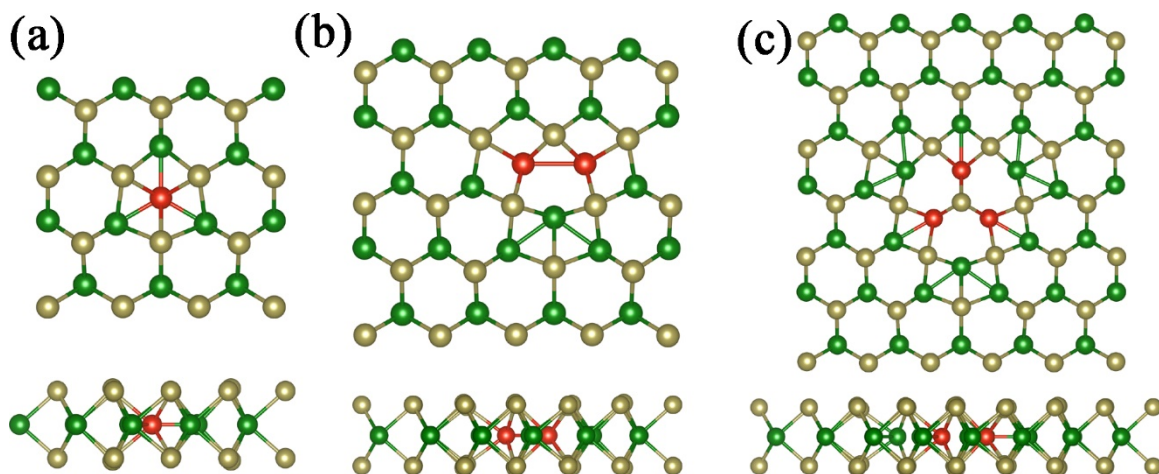


**Figure S5.** Representative atomic models of (a) one, (b) two and (c) three interstitial V atoms in  $\text{MoTe}_2$  layer.

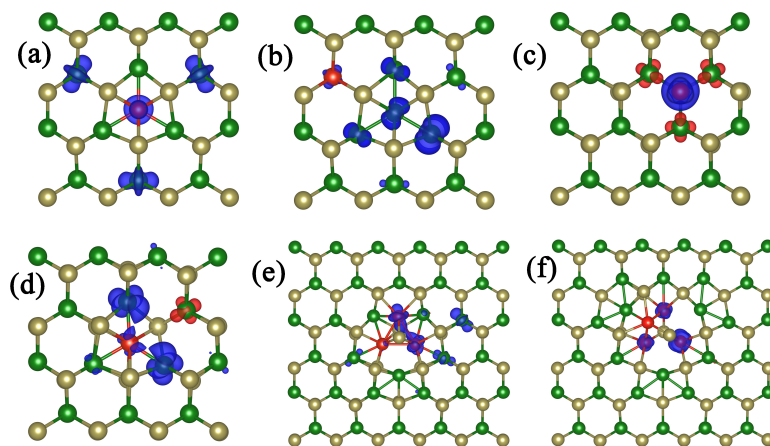


**Figure S6.** Spin-polarization distribution for (a) V interstitial, (b) imp.-Int.-2, (c) V at Te site, (d) V at Int. with Te defect (e) Sur.-Comp-3 and (f) Sur.-Comp-4 configurations.

**Table S1: Formation energy ( $E_f$  in eV) and magnetic moment ( $M$  in  $\mu_B$ ) of different atomic configurations of Ti and V atoms in  $\text{MoTe}_2$  layer.**

S.No.	Configuration	Ti		V	
		$E_f$ (eV)	$M$ ( $\mu_B$ )	$E_f$ (eV)	$M$ ( $\mu_B$ )
1.	Top-H	-0.116	3.86	-0.595	5.00
2.	Top-Mo	-0.555	4.00	-1.126	5.00
3.	Interstitial	-3.139	0.00	-3.569	1.00
4.	Imp. Int.1	-3.332	0.00	-2.947	0.00
5.	Imp. Int.2	-3.158	0.00	-2.735	1.00
6.	Split Int.	-0.029	0.00	-0.626	0.00
7.	Imp. Split Int.	-1.013	0.00	-0.754	1.00
8.	M at Mo site	-0.972	1.00	-1.153	0.00
9.	Sur.-Comp.-1	-1.651	1.91	-1.884	0.00
10.	Sur.-Comp.-2	-3.012	0.00	-3.227	0.00
11.	Sur.-Comp.-3	-4.084	0.00	-4.043	1.00
12.	Sur.-Comp.-4	-4.033	1.00	-3.876	1.64
13.	M at Te site with a Te Defect	-4.248	0.00	-3.758	1.00
14.	M at Int. with a Te Defect			-3.845	1.00

The lowest energy conformation of Ti and V metal atoms in  $\text{MoTe}_2$  layer are found by comparing energies of three ad-atom, one surface complex, and five interstitial type configurations. The ad-atom configurations are namely, Top-H, Top-Mo, and Top-Te configurations in which the Ti/V atom is adsorbed on top of hollow site(interstitial), Mo site, and Te site, respectively. Te-top configuration is not stable for both Ti and V atom and it is converged into Mo-Top configuration. This configuration is denoted as surface complex (Sur.-Comp.-1V) structure. In other five configurations, the Ti/V atom is inside the  $\text{MoTe}_2$  layer. In the interstitial configuration, the Ti/V atom occupies the hollow site. Whereas in the impurity interstitial configurations, the Ti/V atom occupies the Mo site and the Mo atom is displaced to first (Imp.-Int.-1) or second (Imp.-Int.-2) nearest neighbor interstitial site. In the split interstitial configuration, the Ti/V atom occupies Mo site along with the Mo atom to form Mo-Ti/V dimer. Similarly, Imp. Split Int. configuration has Ti/V atom at Mo site with a displacement of Mo atom to form a  $\text{Mo}_2$  dimer in a nearest neighbour Mo site.

All energies are presented in Table S1, from which it is clearly evident that the interstitial configurations are more stable than the ad-atom configurations. Among the ad-atom configurations, the Top-Mo configurations of Ti and V atoms are 0.44 and 0.53 eV lower in energy (that is the configuration are more stable) than the respective the Top-H configurations. Interestingly, it is found that the Sur.-Comp.-1 is 1.096 eV and 0.758 eV lower in energy than the Top-Mo of Ti and V atom, respectively.

The barrier of the V atom to move from Te site to the interstitial site is 40 meV, which can be overcome at room temperature. Thus the surface complex may have one or more V atom at the Te and interstitial sites with a Te atom protrusion. Such complex structures have been reported in Figures S4 and S5. Among the surface complex structures, the 4V complex has maximum magnetic moment of 3.00  $\mu_B$ . The Sur.-Com.-4V has the maximum size of the complex possible with 3V atoms filling the interstitial sites and a Te capped V atom at the Te site. The ground state interstitial configuration has 1  $\mu_B$  magnetic moment. The spin polarized

calculations revealed that the total magnetic moment is distributed over V atom and the three nearest neighbor Mo atoms. The V and each of nearest neighbor Mo atoms carry  $0.33 \mu_B$  and  $0.186 \mu_B$  magnetic moment, respectively. To get more insights into the magnetism, the spin polarization density is plotted in Figure S6, which clearly shows that the magnetic moment is originating from the  $d_z^2$  orbital of V and Mo atoms.

For Ti atom, the “Imp. Int. 1” configuration in which the Mo atom is displaced to second-nearest-neighbor hollow site, is the ground state configuration, and it is 0.174 eV lower in energy than the normal interstitial configuration. All the Ti impregnated structures are nonmagnetic. Only the unstable structures such as Top-Mo, Top-H and Sur.-Comp show magnetic moments.

After annealing of the sample, mirror twin boundaries have been formed in the sample. They are non-magnetic, according to our calculations. Therefore, MTB loops are modeled to understand the role of V on the MTB structures. The V atoms are substituted at Mo sites of the MTB loop. It is found that the V atom prefers to be at the corners of the MTB loop. However, the energy difference between the corner site and edge is 0.318 eV, which is very small. We have also substituted V outside the MTB loop, but it is 0.488 eV higher than the corner site. Interestingly, there is no magnetism observed from the V-doped MTB loops. Thus, it is concluded that V atoms will prefer to be in the MTB loops, which quenches magnetism. Similar conclusions have been drawn for Ti doped MTB loop structures.

### Migration barriers

To get more insights into the dynamical growth of V-incorporated  $\text{MoTe}_2$ , we calculated the barrier energies involved in the diffusion of V atom from the Mo-Top to Interstitial site and H-Top to interstitial site. The barrier for H-Top-Interstitial path is 0.563 eV, while the former has a slightly higher barrier of 0.783 eV. Thus, an ad-atom will prefer the H-Top-interstitial path only if the barrier for the surface diffusion is low enough. So the diffusion barrier for moving from Mo-Top to H-Top is also calculated to be 0.582 eV, which is larger than 0.051 eV required for a back-diffusion of V atom from the H-Top to Mo-Top sites. Thus, the V atom is likely to diffuse from Mo-Top to interstitial site directly, as its life time is very small at the H-Top site.

Migration path from one Mo-Top site to the neighboring one also proceeds via H-Top site, and thus the migration barrier for adatom diffusion is 0.582 eV.

Barrier for migration of the V atom from the Te-site to interstitial site (thereby leaving behind a Te vacancy) is 0.488 eV.

The calculated barriers for Ti atoms are considerably smaller as compared to that of V, and thus Ti atom can move easily inside the layer. For the Mo-Top-Interstitial and H-Top-Interstitial configurations, the barriers are 0.328 and 0.277 eV, respectively. Interestingly, the surface diffusion barrier for Top-Mo to Top-H is 0.510 eV, which is significantly larger than in-diffusion barriers. Thus, the Ti atom will be absorbed inside the layer, rather than moving on the layer.

## Density of states

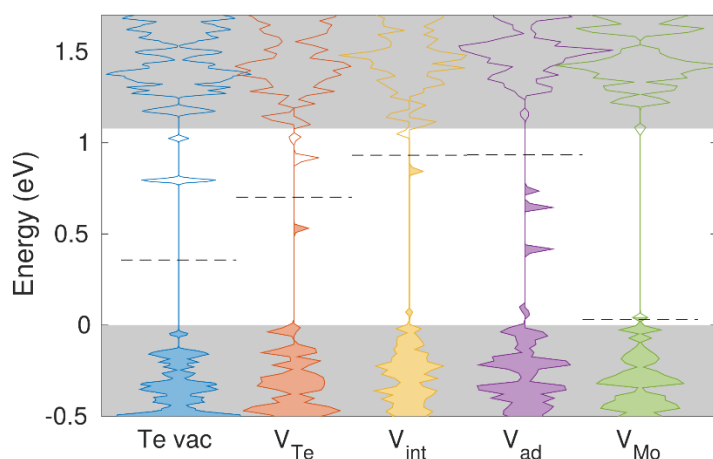
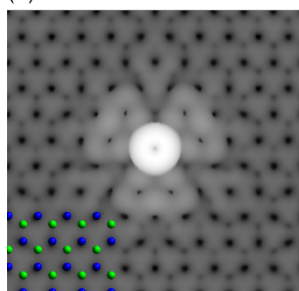


**Figure S7** Total density of states for Te vacancy, V at Te site, V interstitial, V adatom and V at Mo site defects. The Fermi-level is depicted by a horizontal dashed line and furthermore the occupied/unoccupied states are drawn filled/empty. The gray areas denote the valence and conduction band states as extracted from pristine  $\text{MoTe}_2$ . The energy zero is set to valence band maximum.

The density of states for the selected defects are shown in Figure S7. Te vacancy has empty states at about 0.8 eV above VBM and is thus a deep acceptor. V interstitial and V adatom defects have occupied states high in the gap and are thus donors. In particular, the occupied state of V interstitial is slightly above the empty state of Te vacancy and thus charge transfer may occur when both defects are present. V at Te site has both occupied and unoccupied states in the gap and thus could behave as an amphoteric defect. V at Mo site is a shallow acceptor, as expected.

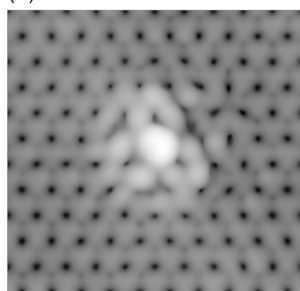
## STM images

(a) V at Te site + Te adatom

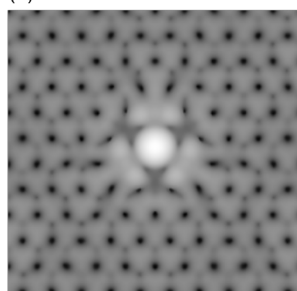


Mo Te

(b) 3 V interstitial



(c) Mo at Te site



(d) V at Mo site, -1 charge

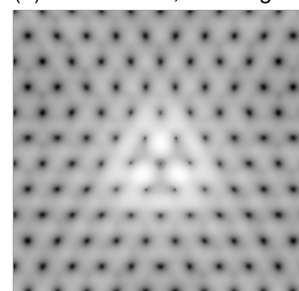


**Figure S8.** Simulated STM images for (a) V at Te site with a capping Te adatom, (b) 3 V at interstitial sites, (c) Mo at Te site, and (d) V at Mo site in -1 charge state.

STM images for few additional configurations are shown in Figure S8. The simulation parameters are the same as before. Since the V-at-Mo-site defect is a very shallow acceptor, it will become -1 charged in our n-type samples.